Twin surface dielectric barrier discharge for pulsed atmospheric plasma production using novel interfractal electrodes

Wymenga, L.F.A.; van Turnhout, J.; Ghaffarian Niasar, M.; van Zeijl, H.W.; van Driel, W.D.; Zhang, G.Q.

DOI
10.1088/1361-6463/ae2aef

Publication date
2025

Document Version
Final published version

Published in
Journal of Physics D: Applied Physics

Journal of Physics D:
Applied Physics

PAPER • **OPEN ACCESS**

Twin surface dielectric barrier discharge for pulsed atmospheric plasma production using novel interfractal electrodes

To cite this article: L F A Wymenga *et al* 2026 *J. Phys. D: Appl. Phys.* **59** 025203

Journal of Physics D: Applied Physics

OPEN ACCESS

RECEIVED
17 October 2025

REVISED
2 December 2025

ACCEPTED FOR PUBLICATION
10 December 2025

PUBLISHED
30 December 2025

PAPER

Twin surface dielectric barrier discharge for pulsed atmospheric plasma production using novel interfractal electrodes

L F A Wymenga[1,*], **J van Turnhout**[2], **M Ghaffarian Niasar**[3], **H W van Zeijl**[1], **W D van Driel**[1] and **G Q Zhang**[1]

[1] Electrical Components, Technology and Materials, Delft University of Technology, Delft, The Netherlands
[2] Materials Science and Engineering, Delft University of Technology, Delft, The Netherlands
[3] High Voltage Technologies, Delft University of Technology, Delft, The Netherlands
[*] Author to whom any correspondence should be addressed.

E-mail: l.f.a.wymenga@tudelft.nl and m.ghaffarianniasar@tudelft.nl

Keywords: cold atmospheric plasma, DBD, interfractal electrode, alumina PCB, unipolar nanopulses, reactive oxygen and nitrogen species

Supplementary material for this article is available online

Abstract

Cold atmospheric plasma (CAP) is widely used in domains such as disinfection, surface treatment and food preservation. When generated in air, CAP is rich in reactive oxygen and nitrogen species (RONS), such as ozone (O_3). A dielectric barrier discharge (DBD) is a reliable method to create CAP. We developed a double-sided (twin) surface DBD with novel 'interfractal' electrode geometries. This fractal configuration creates stronger electric fields than the customary interdigital line geometry. So, CAP is produced more effectively, resulting in higher RONS concentrations. The performance of interfractal electrodes was compared to that of interdigital electrodes (IDE) in atmospheric air. Nanopulsed powering was used, since it is the most efficient for powering DBDs. Electrical and chemical characteristics (such as ozone level) were assessed. The results show that interfractal electrodes enhance the electric field, conduction current and ozone yield.

1. Introduction

Cold atmospheric plasma (CAP) is a partially ionized gas at ambient pressure and near-room temperature. It contains electrons, positive and negative ions, (UV) photons, neutral species, and reactive species [1–3]. 'Cold' indicates that its temperature remains close to room temperature, typically not exceeding 100 °C [1, 2]. This contrasts sharply to a thermal plasma (such as that in the sun), which can reach millions of degrees Celsius. CAP remains cold because only partial gas breakdown occurs. It consists of many transient microdischarges, lasting only 1–10 ns, with a diameter of 100 nm and a length of a few mm [4]. Between the microdischarge events, the air cools down rapidly.

CAP is initiated by a strong electric field in an atmospheric gas. When this field becomes sufficiently high (~3 kV mm^{-1} in air), dielectric breakdown takes place and (background) electrons will be accelerated, thereby colliding with oxygen and nitrogen molecules to form reactive oxygen and nitrogen species (RONS) [4].

Historically, the first CAP was produced by W. von Siemens in 1857, who used a coaxial DBD driven with AC [4, 5]. However, the earliest observation dates back to 1785, when Van Marum used a corona discharge and noticed 'a weird odor' [5]. This was most certainly the distinct smell of ozone (O_3), one of the key RONS formed in air. CAP has since found multiple applications such as surface treatment [6], food preservation [7], disinfection [8], gas flow cleaning [9] and water treatment [10].

Several electrical configurations, such as a dielectric barrier discharge (DBD), a corona discharge or a plasma jet can yield CAP [11]. The optimal configuration depends on the intended application. For example, a plasma jet generates intense plasma spots, useful for surface treatment [12]. By contrast, a DBD covers a much larger area. A corona discharge can be powered with DC, AC or pulses, whereas a plasma jet and a DBD require AC or pulses, as they have an insulating dielectric barrier between the live

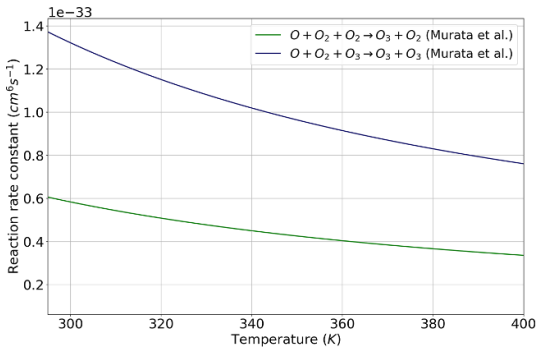

Figure 1. Ozone formation reactions, and their reaction rate constants, plotted vs. the microdischarge channel temperature, according to the reaction rate constants given by Murata *et al* [24].

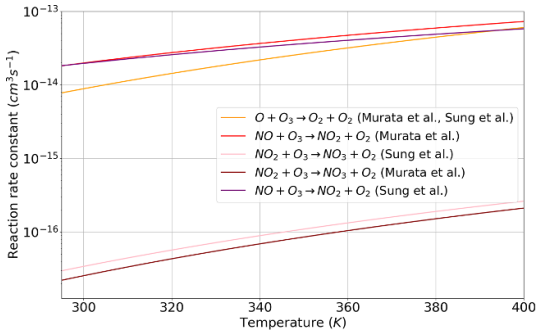

Figure 2. Ozone decomposition reactions, and their reaction rate constants, as a function of the microdischarge channel temperature. The plots visualize the exponentials given for the rates by Murata *et al* [24] and Sung and Sakoda [23].

and grounded electrode. This barrier prevents arcing, i.e. the transition from partial to full breakdown of the surrounding gas, which would trigger a hot thermal plasma (such as lightning) [11].

A DBD plasma source can be designed in various ways to improve its efficiency. For example, sharp electrodes increase the local electric field [13]. Then, a plasma emerges at lower voltages (because the breakdown voltage V_{br} decreases). A thinner dielectric barrier also reduces the breakdown threshold [14–16], while longer electrodes expand the discharge area [16–18]. The RONS composition can be tuned somewhat. Cimerman *et al* (and others) identified two operational modes of a DBD in air, namely the 'O_3 mode' (ozone dominant) and the 'NO_x mode' (nitrogen species dominant) [19, 20]. The microdischarge channel temperature plays a key role in these operational modes [19, 21, 22]. When the microdischarge channel temperature rises, ozone formation is suppressed and its decomposition accelerated, leading to a lower ozone concentration [23, 24]. This phenomenon is known as 'quenching', and may result from a (too) high plasma power density, which was observed already by Warburg *et al* in 1906 [25, 26]. Figures 1 and 2 represent the exponential temperature dependence of some ozone formation and dissociation rate constants put forward in [23, 24].

When a voltage is applied to a DBD electrode, an electric field is established in the surrounding air. For efficient CAP production, it is beneficial to create the highest electric field possible, with the lowest voltage. Then, the high voltage power electronics can be relatively lighter, cheaper etc. A similar approach was tried in the work of Kim *et al* [27]. Also, less power is then converted into heat. This helps to operate the DBD in the desired O_3 mode across a wider parameter range (such as applied voltage, frequency, gas temperature) [19, 28].

Fractals are mathematical constructs with unique properties, described comprehensibly by Mandelbrot [29]. They are self-similar patterns ('curves without tangents') that can be scaled indefinitely, which results in complex shapes. Astoundingly, many of these patterns are found in nature, such as coastlines, snowflakes and tree branches [29].

Earlier studies have shown that fractal electrodes intensify the local electric field. This is attributed to the 'edge-effect' or 'corner-effect'. There are more edges (corners) in a fractal electrode than in a parallel line or comb electrode of equal length [30–33]. These studies highlight the advantage of fractal over line electrode devices for several applications.

Alduais *et al* used space-filling fractal electrodes for electrodynamic screens [33]. These screens repel dust from surfaces, and are used for self-cleaning solar panels. The authors showed that fractal electrodes consume less power than interdigital electrodes (IDEs). Charan *et al* used space-filling electrodes in micro-heating panels to achieve a more uniform temperature distribution compared to line electrodes [34]. Hota *et al* applied fractal electrodes in microsupercapacitors and found that fractal capacitors have a better charge storage than IDE ones [30]. Favorable results were likewise obtained by Anagha *et al*, Yang *et al* and Syed *et al* [31, 32, 35]. Pei *et al* found that fractal electrode nanosupercapacitors outperformed IDE ones [36]. They show that (high order) fractals increase the interfacial area of the electrodes, and strengthen the local electric fields due to small electrode gaps and edge effects [36]. A higher number of corners increased the capacitance, and these effects were consistently observed down to nanometer-scale electrodes.

Surprisingly, no publications have yet appeared about CAP production with fractal electrodes. Therefore, we discuss such electrodes in this article. In a surface DBD, a dielectric barrier separates the live and grounded electrode(s). So, when complementary fractal electrodes are implemented, the fractals must be separated by this barrier. We noticed that fractal patterns can be converted to achieve this. Normally, the mathematical procedure to create a fractal will result in a pattern consisting of a single curve. However, the area around this curve can be divided in two adjacent, non-connected tracks for space (or plane)-filling fractals (such as the Peano, Moore or Hilbert curves). If these tracks are chosen as electrodes, we obtain two distinct electrodes which both have a fractal pattern. The original fractal path now serves as insulating space between these electrodes. The two fractal electrodes meander around each other without touching, maintaining a constant gap throughout. We call this an '*interfractal*' pattern. The scalability of fractals gives a lot of design freedom. We can adjust the spacing between the interfractal electrodes, the electrode width as well as the number of repetitions or iterations (called 'order'). Several other authors have adopted these 'interfractal patterns' of space-filling fractals [30, 36] without noting it, only Tiliakos *et al* call it *'affine transformations'* [37]. All prior implementations placed both interfractal electrodes on the same plane. We propose a twin-plane design and place them on opposite sides of a ceramic printed circuit board (PCB), so on dual planes in the z-direction.

This study introduces interfractal electrodes for CAP production for the first time. While double-surface (or twin) surface DBD (sDBDs) were used before, they did not contain fractal electrode geometries [9, 18, 38–43].

A double-sided ceramic surface DBD was built by printing two silver interfractal Hilbert electrodes (7th order). For comparison, a matching IDE DBD was made with the same electrode width and spacing. Both DBDs were driven in ambient air by high-voltage nanopulses. Chemical characteristics were determined by ozone (O_3) measurements and optical emission spectroscopy (OES). Electrical performance was evaluated by voltage and current measurements, as well as light emission and photomultiplier tube (PMT) analysis.

2. Method

2.1. DBD design and fabrication

We chose to use a Hilbert space-filling fractal since it contains the most corners per surface area, compared to other space-filling fractals (Peano, von Luxburg, R space) [36]. We found that the order of the Hilbert fractal could be extended up to the 7th order (see section 3.1). This vastly increased the number of corners per surface area, because the number of segments grows from 3 to 16 383, when the order is raised from 1st to 7th (see equation (1)). A 7th order Hilbert fractal pattern can be visualized in Wolfram Mathematica (13.3) with the following command:

Graphics[{Thickness[0.005], HilbertCurve[7]}]

The Hilbert pattern (figure S5) was exported to Inkscape (v. 1.2), where it was used as a template to draw both aligned interfractals as a scalable vector graphics (*.svg)* file (figure S6). This allows scaling and mapping of the pattern onto a defined grid, so that the electrode spacing and size could be precisely set. The pattern was next exported as *.dxf* file to Altium Designer (v. 20.2.4), where the PCB layout was finalized, and the electrode width set. The patterns were scaled to fit on the dielectric barrier, an alumina (Al_2O_3, 96% pure) plate of 100 × 100 × 1 mm (l × w × h). The insulating fractal path followed the original Hilbert curve (figure 3). The parallel line pattern was a stereotype interdigital pattern (figure 3). The spacing between the top and bottom electrodes was 0.5 mm and the electrode width 0.25 mm in both DBDs. The two interfractal electrodes were placed on separate sides (top-bottom) of the ceramic barrier (figure 3). The IDEs were similarly placed. The total electrode area was

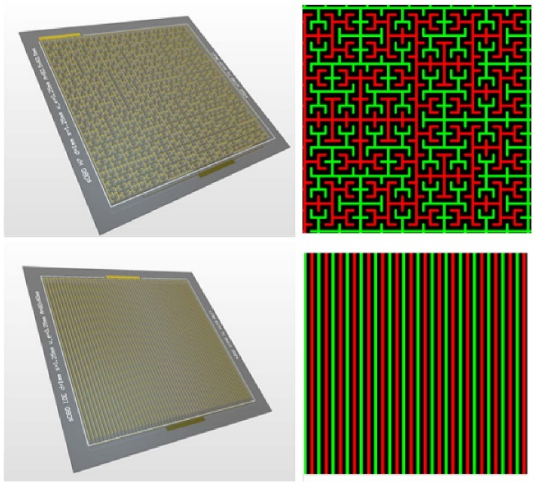

Figure 3. Twin surface DBD plasma panels. Top left: Interfractal DBD. Top right: Schematic of Hilbert interfractal electrodes. Bottom left: IDE DBD. Bottom right: Schematic of interdigital electrodes. Red color: top electrode, Green color: bottom electrode. Black color: spacing between electrodes. For the interfractal Hilbert electrodes, the black track coincides with the original fractal path.

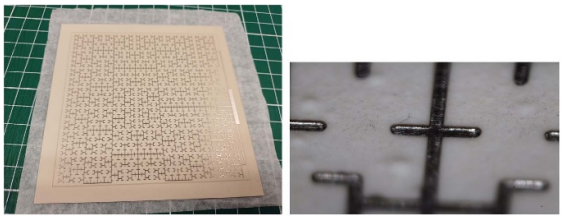

Figure 4. Left: Manufactured ceramic (Al_2O_3) twin surface DBD with interfractal Hilbert 7th order electrodes (Ag/Pd). On the right hand side of the PCB, a connection pad for soldering the HV wires is present. Right: Close-up of the electrode traces.

82.5 × 82.5 mm^2 per side (figures S7 and S8). The ceramic PCBs were produced by CerCuits, Belgium. Al_2O_3 was chosen as barrier because of its high dielectric strength, ozone resistance, and good thermal properties compared to standard FR-4 PCB material [44–46]. The electrode material was 30 μm-high silver/palladium, which has a low resistance, minimal electron migration and good solderability. A connection pad was designated on each side of the DBDs for soldering the high voltage cables (see figure 4).

The total number of segments l of a Hilbert fractal can be calculated from [47]:

$$l = 4^n - 1 \tag{1}$$

where n is the fractal order. This gives a total arc length of 16383 segments for the 7th order Hilbert fractal. In our design, each segment was 0.75 mm long. Because of this length, the insulating Hilbert-7 fractal path exceeded the available electrode area of 82.5 × 82.5 mm. The fractal pattern was therefore cut short by 26.1%. Its active length thus amounts 16383 × 0.75 × 0.739 = 9080 mm. This results in a length of ∼9 m on each side. The IDE DBD had a similar electrode length. It consisted of 55 tracks of 82.5 mm long on both sides, which add up to 55 × 82.5 × 2 = 9075 mm.

2.2. Experimental setup

A 3D-printed frame was made from PETG filament, which has good ozone resistance (see figure S4). This frame, equipped with four nylon pillars, lifted the DBDs from the ground without touching the electrodes. It should be recalled that plasma will form on both sides of the barrier. The DBD was housed in a sealed PMMA box of 270 × 270 × 60 mm (with an air volume of ∼4.3 l). The ozone build-up in this box was measured using a chemical ozone meter (SKY2000-WH-O3, YuanTe Tech. Co., 0–500 ppm). Air was drawn at a calibrated flow rate of 0.6 l min^{-1} through the chemical sensor, which was connected via a PTFE tube to the air outlet of the PMMA box. Two additional holes in the box allowed the HV cables to pass through, while simultaneously acting as air inlets (see figure S4).

The cables were connected to a high-voltage push-pull switch (Behlke GHTS100A, with protective series resistor of 200 Ω, figure 5). This switch produces square nanopulses of varying length

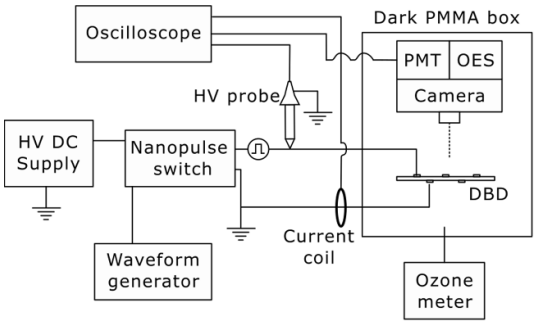

Figure 5. Schematic of test setup.

($t_{pulse} \geqslant 100$ ns), voltage (1–10 kV) and pulse repetition frequency (PRF, 0–15 kHz). In this study, t_{pulse} was 1000 ns, PRF was 100/500 Hz and the positive pulse voltage was 0–6 kV.

The pulses have a rise time of 23 ns or longer (depending on the capacitive load of the plasma device). The capacitance was found to be 192 and 195 pF for the inactive interfractal and IDE DBDs, respectively (Keysight U1733C LCR meter).

The HV-switch was powered by a positive DC supply (Spellmann SL40PN600, 0–40 kV, 0–15 mA) equipped with voltage and current displays. 5 V pulses were fed to the switch by a signal generator (Tektronix AFG3252C). The pulses at the high voltage output of the switch were measured with a 1:1000 high-voltage probe (Tektronix P6015A, 10 ft. cable). The current was recorded at the ground electrode of the plasma panel with a 1:20 current coil (Pearson 3525, connected with 50 Ω termination).

A PMT (Thorlabs PMT1001/M) was connected to a laptop with manufacturers software (PMT2100 v4.0, settings: gain 1.0, offset −1.5 V, resolution 80 MHz). The PMT was mounted 50 mm above the plasma panel with a grounded clamp, and connected to the oscilloscope with 50 Ω termination. A neutral density filter on the PMT (Thorlabs NDUV40A) reduced the incoming light intensity by 99.99% over the whole wavelength range.

Photographs were taken by placing a camera 100 mm above the plasma panel (Nikon Z7 II with Nikkor 24-120/4 S lense, ISO25600, shutter time 0.5 s). The camera was controlled through a wireless module (CamRanger 2, with app). Detailed images of the DBDs were captured with a 3D microscope (Microqubic MRCL700).

An optical emission spectrometer (Avantes Avaspec 3648) was used with AvaSoft 8 software and optic fiber probe (Avantes FC-UVIR600-2), which was calibrated in-house by use of a deuterium-halogen lamp (Avalight-DH-S-BAL). The fiber probe was positioned 30 mm above the DBD. The spectrometer had the following settings: resolution 0.33 nm, detection range 175–1100 nm, slit 10 μm, grating 300 grooves mm^{-1}. The photographs and OES measurements were made in a darkened chamber (GlareOne LED Cube 60) with a blackout curtain placed over the chamber. Temperature and humidity of the air were measured with a sensor probe (Dostmann P670). Surface temperature of the DBD was measured with an infrared meter (Fluke 68 IR).

The output of the signal generator, high-voltage probe, current coil and PMT sensor were monitored by a high-resolution oscilloscope (Rigol MSO5354, 350 Mhz, 8 GSa s^{-1}). All experiments were conducted in an interlocked Faraday cage, with the researcher located outside for safety.

3. Results

3.1. Modeling of electric fields

Electric field modeling was carried out with COMSOL software (v. 6.2, electrostatics package). Silver ($\varepsilon_r = 1 \cdot 10^6$) electrodes were placed on the top and bottom of a 1 mm-thick alumina ($\varepsilon_r = 10$) sheet in air (see figure 6).

We varied the electrode height (h_{elec}), width (w_{elec}) and spacing in a 2D model to evaluate their influence on the maximum electric field E_{max} (3 kV applied on the top electrodes, mesh setting: extra fine). Data, acquired by 'sweeping' these parameters systematically, was processed and plotted in Python (Spyder v.6), see figure 8.

The electrode height did not alter E_{max} (as E_{max} resides near the dielectric surface). But, it extended the region where plasma could be formed (figure 7). Therefore, the maximum production limit of h_{elec} (30 μm) was chosen.

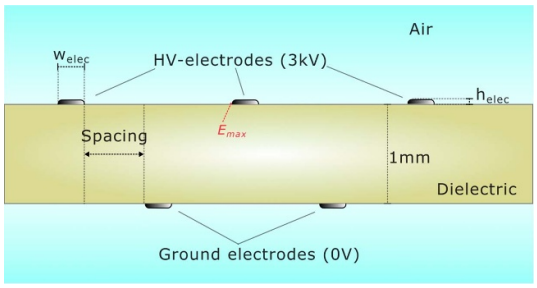

Figure 6. Schematic setup of model. The electrode width and height (w_{elec}, h_{elec} resp.) and electrode spacing were varied. The spot for computing E_{max} was set at 0.5 μm above the dielectric barrier and 0.5 μm left of the central HV-electrode in air, where the electric field was found to be strongest.

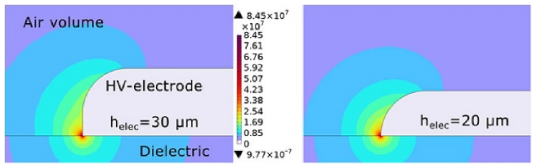

Figure 7. Calculated electric field strength. Left: $h_{elec} = 30$ μm, right: $h_{elec} = 20$ μm.

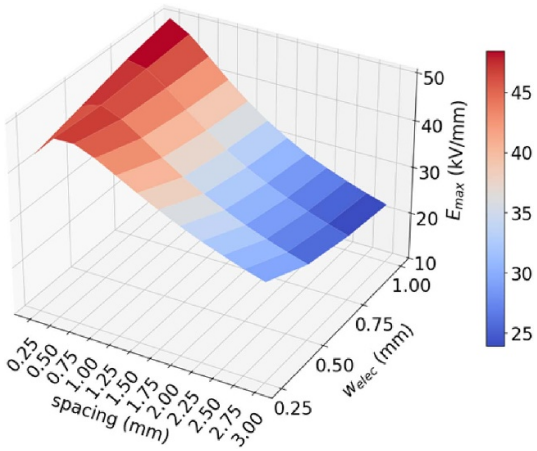

Figure 8. Maximum electric field in the air near the high voltage central electrode ($h_{elec} = 0.03$ mm), as function of electrode spacing and width.

E_{max} increases when the spacing between the top and bottom electrodes decreases (figure 8). However, when the spacing becomes too small (0.25 mm), we see a decline in E_{max} (for $w_{elec} \leqslant 0.5$ mm). This is attributed to field interference between too closely spaced equipotential electrodes [48].

The minimum production limit for w_{elec} of 0.25 mm was chosen to maximize the electrode length within the available area. For this width, we find an optimal spacing of 0.5 mm. Then, E_{max} is merely 5.1% lower than the maximum value found in figure 8 (50.2 kV mm^{-1}). For a spacing of 0.5 mm, the straight segments of the Hilbert curve must each be 0.75 mm wide (see figure 3 top right). When the Hilbert fractal was scaled to these dimensions, a 7th order fractal emerged. The order thus follows directly from the dimensional optimization performed in our modeling. As noted earlier, the order should be as high as possible to maximize the number of sharp corners.

A 3D simulation was performed to compare the electric field between the IDE and interfractal DBD (figure 9). To mimic a twin surface DBD configuration, a top and bottom electrode were placed on an 1 mm-thick alumina substrate (with 3 kV applied to the top electrode, mesh: extra fine). The electric field was mapped along the straight electrode (see figure 9(c), representing the IDE DBD) and at the electrode edge (figure 9(d), representing the fractal DBD). The electric field clearly becomes stronger in

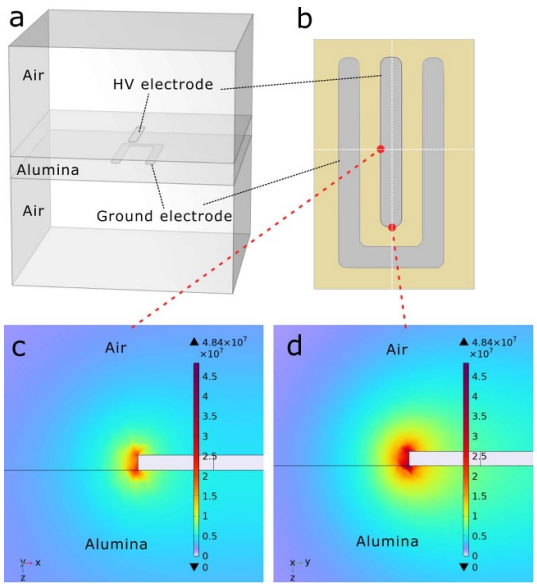

Figure 9. Twin surface DBD modeling of electric field. (a): Model setup. (b): Top view of HV and ground electrode. (c): Electric field distribution (V m^{-1}) along the straight part of the HV electrode. (d): Electric field distribution (V m^{-1}) at the edge of the HV electrode ($w_{elec} = 0.25$ mm, $h_{elec} = 0.03$ mm, spacing = 0.25 mm, applied voltage: 3 kV).

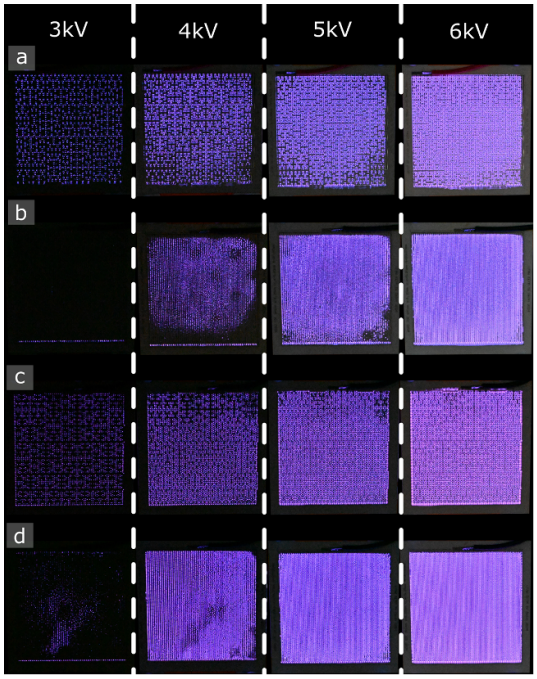

Figure 10. Application of 3–6 kV positive nanopulses to interfractal and IDE DBDs (PRF = 500 Hz). (a): Interfractal DBD, negative streamers. (b): IDE DBD, negative streamers. (c): Interfractal DBD, positive streamers. (d): IDE DBD, positive streamers ($T = 23.8°$ C, RH = 52%).

the air surrounding the electrode edge (with a maximum of $2.4 \cdot 10^7$ vs. $3.6 \cdot 10^7$ V m^{-1} for the straight and edge electrode, resp.). This implies an enhancement by a factor of 1.5.

3.2. Optical characterization

Figure 10 depicts camera pictures of both panels excited by 4 pulse voltages (PRF = 500 Hz). In general, CAP in air produces microdischarge filaments called streamers [11, 49]. Streamers occur simultaneously on both sides of the interfractal DBD (figures 10(a) and (c)) and IDE DBD (figures 10(b) and (d)). A fundamental difference exists between positive streamers (emanating from a positive high voltage electrode towards ground) and negative streamers (from a negative high voltage electrode to ground) [11, 50].

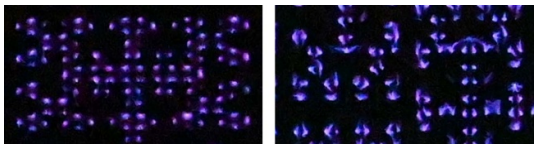

Figure 11. Positive (left) and negative (right) streamers on the interfractal DBD at 3 kV positive pulses. Close-up of figure 10.

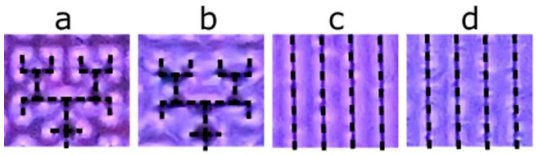

Figure 12. Streamers at 6 kV pulses. (a): Positive streamers interfractal DBD. (b): Negative streamers interfractal DBD. (c): Positive streamers IDE DBD. (d): Negative streamers IDE DBD. Top electrodes are accentuated by dashed black lines (line width = 0.25 mm). Close-up of figure 10.

Positive streamers and negative streamers were observed on resp. The high voltage side and the grounded side of the DBDs (see figures 11 and 12). A clear distinction can be made, positive streamers appeared as many small purple-blue dot-like filaments near the fractal edges, whereas negative streamers showed fewer, more diffuse filaments, which spread further and more unevenly across the alumina surface (figure 11) [51]. Their color was less purplish than that of the positive streamers. The breakdown voltage V_{br} for positive streamers was somewhat lower, which is also reported in [52]. For the interfractal DBD, streamers spread across the whole electrode surface from 3 kV onward, whereas for the IDE DBD this occurred above 4–5 kV (see figure 10). Above 5 kV, the full area of both DBDs was covered with microdischarges (figures 10 and 12).

The enhancement factor of 1.5 (from section 3.1) applies to all sharp corners in the interfractal DBD. We estimated the number of these corners by counting all the streamers visible in figures 10(a) and (c) at 3 kV. They appear at the locations where early breakdown is observed on both sides in the interfractal DBD. The counting procedure is described in the supplementary material. In total, 2922 positive and 2180 negative streamers were identified. So, the interfractal electrodes enhanced the electric field at ~5100 points on the DBD surface, compared to the IDE electrodes.

3.3. VI characteristics

Nanopulsed excitation is increasingly preferred over AC for creating intense CAP [11, 53]. It offers several advantages. First, because of the rapidly changing electric field, the electron energy is increased (compared to AC) due to faster electron acceleration [54]. This results in a higher RONS production, e.g. ozone [55]. Secondly, heating of electrodes and air is lower. The pauses between pulses are relatively long, particularly at a moderate PRF (0–15 kHz). This allows the microdischarge channels to cool down. Furthermore, ions move slowly in nanopulses and therefore the rotational and vibrational excitation of air molecules is modest [56, 57]. Overall, nanopulses produce a more intense plasma at a lower power input, with less heat [53]. It has been reported that nanopulses preserve the electrodes and dielectric barrier, while these may be damaged by AC [38].

The voltage $V(t)$ and current $I_{\mathrm{tot}}(t)$ for the interfractal DBD are displayed in figures 13 and 15 for 64 consecutive pulses. Voltage and current were measured with the standard electrode connection (high voltage on the upper electrode, bottom electrode grounded), as well as with the connection reversed (figures 13 and S4). The voltage and current profiles are identical. This confirms symmetrical charge deposition on both sides of the panel, as expected, since the electrode dimensions and length are almost equal. This is true for the interfractal and the IDE DBD (see figures 13 and S1). Large current peaks (up to 15 A) were observed, attributable to the long electrode length, thin dielectric barrier and sharp electrodes. The so called 'two-spike' current shape is visible, as was reported and well explained in [58].

The total measured current in a DBD consists of two components when $V(t) > V_{\mathrm{br}}$, namely the displacement current $I_{\mathrm{disp}}(t)$ and the conduction current $I_{\mathrm{cond}}(t)$ [58–60]:

$$I_{\mathrm{tot}}(t) = I_{\mathrm{disp}}(t) + I_{\mathrm{cond}}(t). \tag{2}$$

The displacement current originates from the capacitive charging and discharging of the DBD. The conduction current is the (plasma) current flowing through air, driven by rapid acceleration of electrons

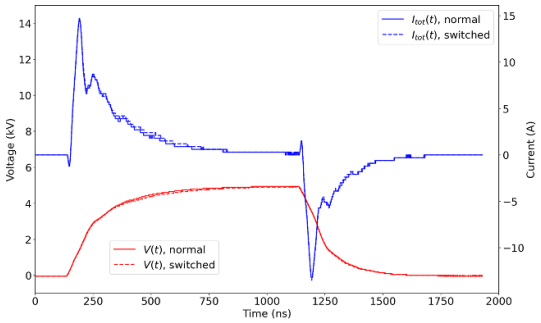

Figure 13. Current and voltage measurement of interfractal DBD, 5 kV pulses, with electrodes in normal and reversed setting (PRF = 500 Hz, T = 22.5 °C, RH = 43%). Data averaged over 64 pulses.

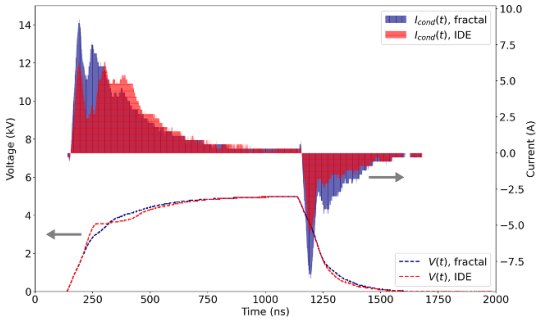

Figure 14. Conduction current $I_{\mathrm{cond}}(t)$ for interfractal and IDE DBD at 5 kV pulses (PRF = 500 Hz, T = 22.7–23.8 °C, RH = 41%−45%, average of 4 measurements, each measurement averaged 64 pulses).

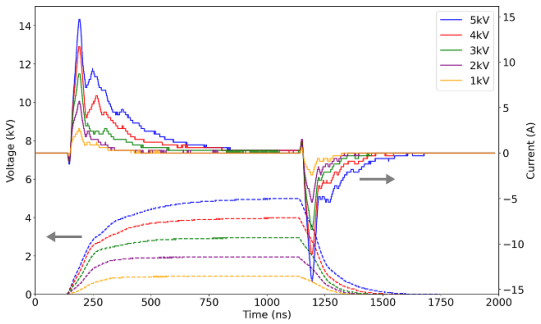

Figure 15. Interfractal DBD total measured current $I_{\mathrm{tot}}(t)$ for pulse voltages from 1–5 kV. Average of 64 pulses, PRF = 500 Hz (T = 23.8 °C, RH = 41%).

and the subsequent electron avalanches. The displacement current was assessed by measuring the total current with $V(t)$ just below V_{br}, which is at 2 kV for the interfractal DBD and at 3 kV for the IDE DBD (see sections 3.2 and 3.4, figure 15). The conduction current can next be estimated from the total current using equation (2). The conduction current (for 64 consecutive pulses) given in figure 14 was slightly higher for the interfractal DBD for 5 kV pulses.

3.3.1. Surface charging

The capacitance of the DBDs (C_{cell}) increased markedly after plasma exposure (PRF = 500 Hz, varying voltages, several minutes). Directly after exposure, the capacitance rose from 190 to ∼530 pF. After 24 h, the C_{cell} decreased to 380 pF and 32 h later to 300 pF. This effect is attributed to the accumulation of surface charge on the dielectric barrier, a phenomenon also observed by others [51, 59]. The capacitance never returned to its pre-exposure value of 190 pF. This is likely due to electrode oxidation, which could be seen on the electrodes. An extra layer of dielectric material (the oxidation layer) forms on the electrode surface. This weakens the electric field in the air gap where plasma is likely generated. Moreover, the electrodes erode, increasing the separation between the electrodes (see figures 21–23). This erosion also limits the electric field in the air next to the electrodes. Between runs, the high voltage side of the

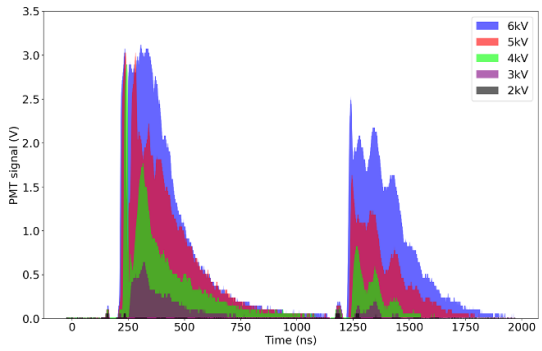

Figure 16. Light emission (PMT-signal) of the interfractal DBD for five pulse voltages (2–6 kV, PRF = 100 Hz, average of 16 pulses).

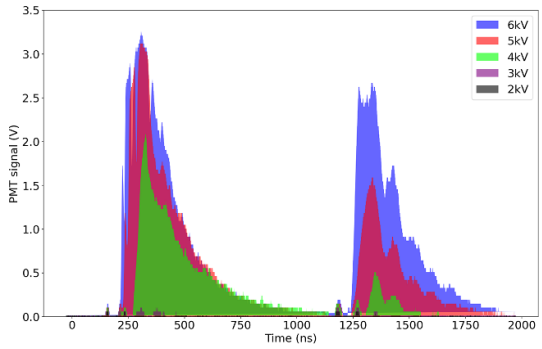

Figure 17. Light emission (PMT-signal) of the IDE DBD for five pulse voltages (2–6 kV, PRF = 100 Hz, average of 16 pulses).

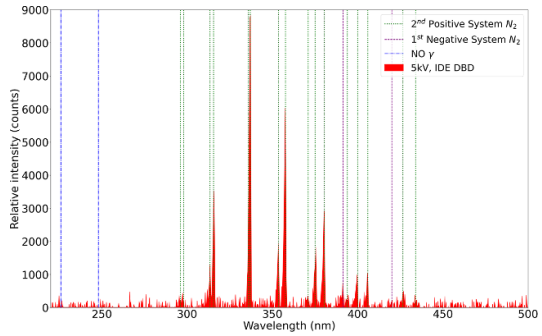

Figure 18. OES spectrum of IDE DBD for 5 kV pulses (PRF = 500 Hz, T = 23.2 °C, RH = 46%). Integration time: 15 s. Average of two measurements after subtraction of a measurement with plasma off (background noise). Vertical lines are the known emission peaks of the first negative and second positive system of nitrogen, as well as the NO γ lines.

DBDs was grounded. Hereby, part of the surface charges may be neutralized. A modest rise in capacitance was observed between the ozone measurement series (from 226 to 307 ± 14 pF for the interfractal electrodes (average of 6 measurements) but this did not significantly modify the voltage and current profiles (see figures S2 and S3) or the ozone production (see section 3.5).

3.4. PMT & OES measurements

PMT measurements revealed the onset of photon emission from interfractal electrodes for ⩾3 kV pulses (figure 16), and from IDE electrodes for ⩾4 kV pulses (figure 17). The measurements were taken on the high voltage side of the DBDs for 16 consecutive pulses. For 1000 ns pulses, distinct primary and secondary discharges were noticed for both DBDs.

The main emission peaks in the OES spectra (figure 18) correspond to the second positive and first negative system of N_2 [61], like other DBDs operated in ambient air [8, 19, 62]. The operation mode is further discussed in section 3.5.

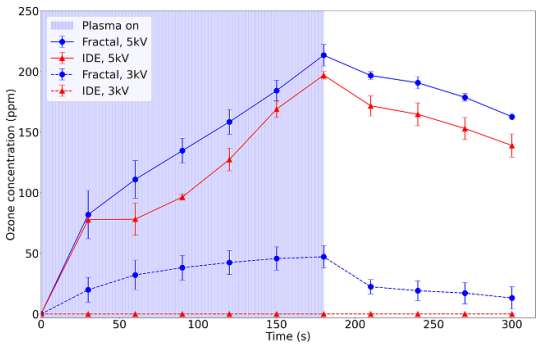

Figure 19. Ozone concentration of the interfractal and IDE DBD for 3 and 5 kV pulses (PRF = 500 Hz, $T = 22.7\,^{\circ}\mathrm{C}-23.8\,^{\circ}\mathrm{C}$, RH = 41%−45%, average of 4 measurements).

3.5. Ozone measurements

The ozone concentration was quantified repeatedly in both DBDs, for 3 and 5 kV pulses (see figure 19). Each measurement cycle lasted 5 min, and four repetitions were conducted per measurement. The plasma was active during the first 3 min, and ozone concentration was recorded every 30 s. After each run, the box was vented for >10 min to reset the ozone level to 0 ppm, while the DBD surface cooled back to ambient temperature (23.5 °C). Directly after the 5 min experiments, the interfractal and IDE surfaces had a temperature of 28.1 ± 0.3 and 28.4 ± 0.3 °C (average of 4 measurements).

The optical observations in sections 3.2 and 3.4 revealed that $V_{\mathrm{br}} < 3$ kV for the interfractal DBD and $V_{\mathrm{br}} > 3$ kV for the IDE DBD. Hence, ozone should be detectable for the interfractal DBD at 3 kV pulses, but not for the IDE DBD. Indeed, no rise in ozone concentration was detected for the IDE DBD at 3 kV, whereas the interfractal DBD produced a concentration of 47 ± 9 ppm after 3 min (average of 4 measurements). For 5 kV pulses, both DBDs show microdischarges over the whole electrode area (figure 10). We measured a maximum ozone concentration of 214 ± 9 and 197 ± 3 ppm for the interfractal and IDE DBD, respectively (average of 4 measurements).

Ozone yield (η_{O3}, in g kWh^{-1}) was calculated using equation (3) [63]:

$$\eta_{\mathrm{O3}} = \frac{60 \cdot C \cdot Q}{P_{\mathrm{plasma}}} \tag{3}$$

where C is the ozone concentration (in g Nm^{-3}), Q the air flow rate (in standard liters per minute) and P_{plasma} the power deposited in the plasma (in W). The latter is given by [63]:

$$P_{\mathrm{plasma}} = \mathrm{PRF} \cdot E_p = \mathrm{PRF} \cdot \int_0^T V(t) \cdot I_{\mathrm{tot}}(t)\,\mathrm{d}t \tag{4}$$

where E_p is the energy per pulse and T the pulse period (see figure 20). The ozone yield was determined for both DBDs using the curves of figure 19 and the corresponding the V–I plots given in figures S2 and S3. The yield amounted to 6.41 and 4.75 g kWh^{-1} for the interfractal and IDE DBD, respectively, indicating that the interfractal DBD increased the ozone yield by 35%. P_{plasma} equaled 2.38 for the interfractal DBD and 2.95 W for the IDE DBD. Although E_{p} was larger for the IDE DBD (see figure 20), a greater portion was diverted to the displacement current rather than the conduction current (which is consistent with the higher V_{br}). This, in combination with the lower ozone concentration, explains the lower yield for the IDE DBD. The input power of the DC supply fed into the nanopulse switch averaged 10.0 and 10.6 W for the interfractal and IDE DBDs, respectively (11 measurements).

The specific input energy (SIE, in J L^{-1}) was calculated from [63]:

$$\mathrm{SIE} = \frac{60 \cdot P_{\mathrm{plasma}}}{Q} \tag{5}$$

and found to be 258 for the interfractal DBD and 320 J L^{-1} for the IDE DBD.

The DBDs operated in the ozone mode throughout the test procedure (5 min). This conclusion is supported by several observations. Firstly: Dry semi-quantative test strips (Macherey–Nagel Quantofix) were placed in the closed box. After the experiments, the strips were wetted with demi-water and the

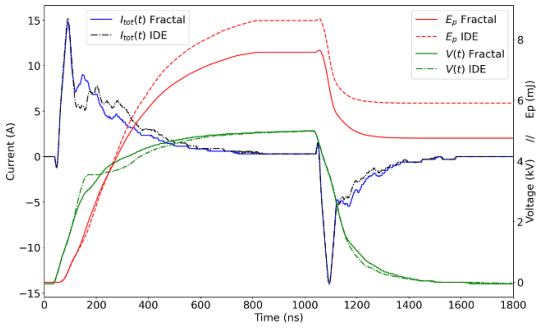

Figure 20. Energy per pulse during ozone experiments. Each curve is the average of 320 pulses.

nitrate (NO_3^-) and nitrite (NO_2^-) concentrations were assessed. Low levels of nitrite and nitrate are expected when a DBD is in ozone mode [20, 22], since these form when NO_x dissolves in water [64]. This was indeed the case for both DBDs, equal values were found (NO_3^- ~ 50 mg l^{-1} and NO_2^- ~ 1 mg l^{-1}, see figure S11). Secondly, the ozone concentration increased steadily over time. A transition towards NO_x would only occur when the concentration flattens or decreases during operation [25]. Thirdly, the electrode heating remained very low (<5°). This was anticipated as the DBDs operated with a low power density characteristic for ozone mode (<0.025 W cm^{-2}) [25]. When electrodes heat up, a shift towards the NO_x mode is likely, see [21, 22]. Fourthly, other authors show that the SIE applied in our DBDs fall in the range associated with ozone mode [19, 63]. We performed our experiments at a moderate air flow and humidity, which suppress ozone destruction and prevent a shift to NO_x mode [19].

4. Discussion

Interfractal electrodes can be deposited just as easily as traditional IDEs on a PCB, thanks to modern computer-aided manufacturing.

To our knowledge, this is the first report on double-sided (twin) surface DBDs utilizing an 'interfractal' electrode pattern. This approach demonstrates that any space-filling fractal (Hilbert, Peano, Moore etc.), of any order, can be split into two non-overlapping fractal electrodes, which can be printed on opposite sides of a dielectric PCB to create a twin surface DBD. The scaling (fractal order) of these electrodes can be adjusted to optimize the performance for a predetermined goal (e.g. capacitive storage, heat dissipation, electric field enhancement).

In our design, an active electrode length of >9 m was achieved on both sides of an Al_2O_3 barrier surface of merely 68 cm^2, based on a space-filling Hilbert fractal (7th order) insulation track. The scaling of the electrodes allows simultaneous formation of many microdischarges, a key factor for effective plasma production [4]. The large electrode length increased the deposited charge and conduction current of the DBD, whereby current peaks up to 15 A were observed (figure 13). We found early streamer formation on ~5100 points on our interfractal DBD as a result (see figures S9 and S10).

It is well-known that sharp or thin electrodes increase the electric field in the air gap (E_g) [65, 66]. Edges or corners are sharper that flat electrodes, and likewise enhance E_g [36]. The breakdown voltage (V_{br}) is thus lowered by the use of sharp electrodes. The electric field enhancement (estimated 1.5x in our interfractal DBD) persists even if $V(t)$ is raised. A higher E_g ramps up the electron temperature and density [67, 68]. This in turn increases the probability of inelastic collisions of an electron with a gas molecule, leading to ionization [69]. This mechanism accounts for the higher ozone concentration in the fractal DBD.

As mentioned previously, a too high E_g in ambient air may cause quenching, leading to decrease of ozone in favour of NO_x production. However, we observed the DBDs to operate consistently in the O_3 regime, cf section 3.5.

The electrode width (w_{elec}) should be minimized to allow a larger number of fractal segments to be put on the barrier, thereby increasing the electrode length. Multiple microdischarges can then be formed simultaneously [4]. Thin electrodes reduce C_{cell} [70]. This shortens the pulse rise time, and lowers the displacement current [71, 72].

Using a thin dielectric barrier (1 mm) increases E_g, relative to thicker barriers [40]. Some authors used a thinner alumina barrier, but this introduces the risk of shattering due to the brittleness of Al_2O_3

Figure 21. Electrode degradation after all experiments described in this study, performed over a span of 2 weeks (left: interfractal DBD, right: IDE DBD). Also, some discoloration of the alumina barrier can be seen, caused by prolonged CAP-induced electron etching.

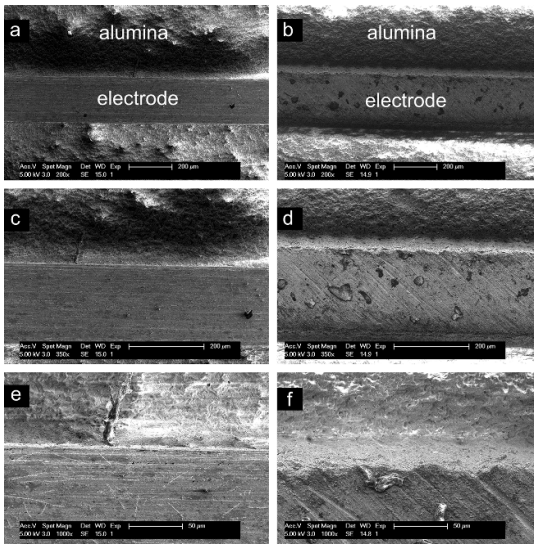

Figure 22. SEM images of unexposed (left) and plasma exposed electrode (right). (a), (b): 200× magnification. (c), (d): 350×. (e), (f): 1000×. Black spots were observed on the exposed electrodes, as well as erosion of the electrode edges. In image f, sputtered particles are observed on the electrode.

[40, 69]. The benefits of alumina are its plasma resistance and high relative permittivity ($\varepsilon_r \sim 10$), which enhance the deposited charge per pulse [73].

Compared to IDE electrodes, interfractal electrodes enhanced E_g due to the abundance of sharp corners and kinks. This translated to a 25% reduction in breakdown voltage for the interfractal DBD (3 vs. >4 kV for the IDE DBD), a 9% higher ozone production and a 35% increase in ozone yield (using positive nanopulses). These findings were supported by current and PMT measurements, which showed a higher conduction current and more photon emission from the interfractal DBD. Li *et al* demonstrated that twin sDBDs produce higher ozone yields than single-sided sDBDs [40]. An interfractal twin sDBD can be seen as a further advancement. While we observed a modest rise (9%) in ozone concentration for 5 kV pulses, the improvement for 3 kV pulses was more striking (47 vs. 0 ppm for the interfractal and IDE DBD resp.). In practice, this means that if the pulse source has a voltage maximum of 3 kV (typical for a solid-state switch device), the interfractal DBD can be powered effectively, whereas the a IDE DBD may not.

However, material considerations remain critical. To prevent electrode or dielectric barrier degradation, all materials in contact with the plasma must be resistant to oxidation, high local electric fields ($\gg$3 kV mm^{-1}) and electron bombardment [74]. Due to technical restrains, only Ag/Pd electrodes could be used, which showed signs of degradation (see figures 21–23). SEM imaging uncovered cracks, eroded areas and signs of electrode material sputtering, compared to unused electrodes (figures 22 and 23). Also, unidentified black spots appeared on the powered electrodes. Although the ozone and current measurements were not affected by this degradation during our experiments (see figures S2 and S3), a reliable long-term operation cannot yet be expected [74, 75]. This limits the industrial implementation of DBDs, because maintenance and replacement are expensive. Electrode erosion may release metal particles in the environment [74]. It also widens the gap between the electrodes, which weakens the electric field. Oxidation layers formed on the electrodes act as extra dielectric barrier, further reducing the electric field. Mitigation strategies include the use of plasma resistant electrodes (such as gold [76]) or

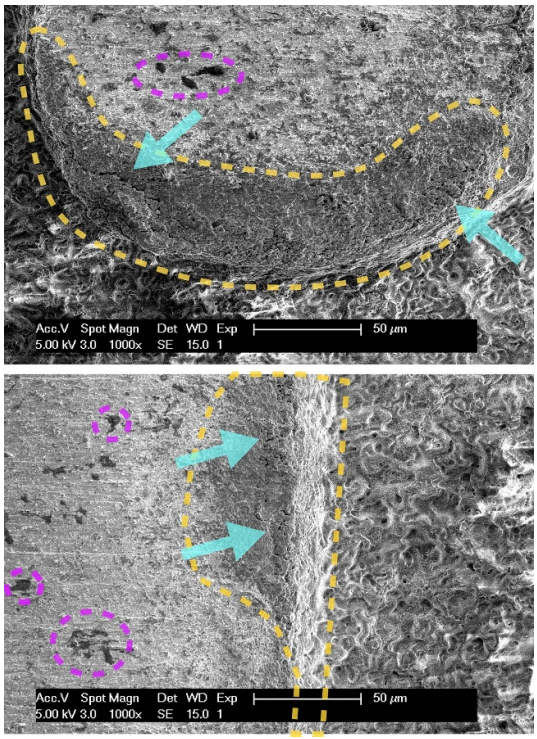

Figure 23. SEM images of the plasma-exposed electrodes. Cracks in the electrodes are accentuated with blue arrows. The yellow encircled area highlights eroded parts of the electrodes. Purple circles accentuate black spots observed on exposed electrodes. Magnification 1000×. Top: fractal edge segment. Bottom: line segment.

embedding of the electrodes within the barrier. The latter strategy has been applied in coplanar [77], grating [78], multi-hollow [63] and volume DBDs [27].

The barrier material (Al_2O_3) showed no signs of degradation, only yellowing [44]. Future research should focus on finding CAP-resistant materials for the fractal electrodes (i.e. gold-plated metals [76] or coatings [27]) and on scaling up to devices with fairly large surfaces (hundreds of cm^2). Whether fractal electrodes degrade faster than an IDE electrodes, might be an interesting topic for future research.

5. Conclusion

A novel fractal-based electrode twin surface DBD (termed 'interfractal DBD') was developed. Compared to an IDE twin surface DBD ('IDE DBD'), the interfractal design produces plasma more effectively.

The interfractal DBD (based on a 7th order space-filling Hilbert fractal) achieved a 9% higher ozone concentration, a 35% higher ozone yield and a 25% lower breakdown voltage compared to a familiar IDE DBD. PMT and current measurements also exhibited a higher photon emission and conduction current for the interfractal DBD.

These improvements are ascribed to the pronounced edge effect in interfractal electrodes. Modeling results indicate that this geometry creates higher electric fields, which in turn raise the electron energy and density, leading to an increased ionization of air. This results in a more power-efficient ozone production. Owing to the stronger edge effect, a higher conduction current and photon emission, as well as earlier streamer formation were observed in the interfractal DBD, all of which support our theoretical interpretation.

Future work of our group will address the observed electrode degradation. This is a critical, underexplored issue for the successful industrial deployment of CAP technologies.

Data availability statement

All data that support the findings of this study are included within the article (and any supplementary files).

Interfractal-twin-sDBD-Suppl available at https://doi.org/10.1088/1361-6463/ae2aef/data1.

Acknowledgment

We thank Stefaan Heirmans for the OES calibration, Fabio Muñoz Muñoz for assistance during the PMT measurements, and Yaqian Zhang for her help with SEM. This research is funded by the Delft University of Technology, the Netherlands, under the PowerizeD project.

Funding

The authors have no conflict of interest to declare. This research is funded by the Delft University of Technology, the Netherlands, under the PowerizeD project.

ORCID iDs

L F A Wymenga 0009-0007-7943-538X
J van Turnhout 0000-0003-4375-8615
M Ghaffarian Niasar 0000-0003-1766-8077
H W van Zeijl 0000-0001-5204-1646
W D van Driel 0000-0001-8882-2508
G Q Zhang 0000-0002-8023-5170

References

[1] Bourke P, Ziuzina D, Han L, Cullen P J and Gilmore B F 2017 Microbiological interactions with cold plasma *J. Appl. Microbiol.* **123** 308–24
[2] Fridman G, Friedman G, Gutsol A, Shekhter A B, Vasilets V N and Fridman A 2008 Applied plasma medicine *Plasma Process. Polym.* **5** 503–33
[3] Radmilović-Radjenović M, Radjenović B, Klas M, Bojarov A and Matejčik S 2013 The breakdown mechanisms in electrical discharges: the role of the field emission effect in direct current discharges in microgaps *Acta Phys. Slovaca* **63** 105–205
[4] Kogelschatz U, Eliasson B and Egli W 1997 Dielectric barrier discharges. Principle and applications *J. Phys. IV* **7** C4–47
[5] Kim H H *et al* 2023 Revisiting why DBDs can generate O_3 against the thermodynamic limit *Int. J. Plasma Environ. Sci. Technol.* **17** e02004
[6] Wegener M, Wirges W, Paajanen M and Gerhard R 2007 Charging behavior and thermal stability of porous and non-porous polytetrafluoroethylene (PTFE) electrets *2007 Annual Report Conf. on Electrical Insulation and Dielectric Phenomena* pp 449–52
[7] Nwabor O F, Onyeaka H, Miri T, Obileke K, Anumudu C and Hart A 2022 A cold plasma technology for ensuring the microbiological safety and quality of foods *Food Eng. Rev.* **14** 535–54
[8] Klämpfl T G, Isbary G, Shimizu T, Li Y F, Zimmermann J L, Stolz W, Schlegel J, Morfill G E and Schmidt H U 2012 Cold atmospheric air plasma sterilization against spores and other microorganisms of clinical interest *Appl. Environ. Microbiol.* **78** 5077–82
[9] Böddecker A *et al* 2022 A scalable twin surface dielectric barrier discharge system for pollution remediation at high gas flow rates *React. Chem. Eng.* **7** 2348–58
[10] Klymenko R, de Kroon E, Agostinho L L F, Fuchs E C, Woisetschläger J and Hoeben W F L M 2024 Characterization of a hyperbolic vortex plasma reactor for the removal of aqueous phase micropollutants *J. Appl. Phys.* **57** 215204
[11] Shao T, Wang R, Zhang C and Yan P 2018 Atmospheric-pressure pulsed discharges and plasmas: mechanism, characteristics and applications *High Voltage* **3** 14–20
[12] Brandenburg R, Becker K H and Weltmann K D 2023 Barrier discharges in science and technology since 2003: a tribute and update *Plasma Chem. Plasma Process.* **43** 1303–34
[13] Lyulyukin M N, Besov A S and Vorontsov A V 2011 The influence of corona electrodes thickness on the efficiency of plasmachemical oxidation of acetone *Plasma Chem. Plasma Process.* **31** 23–39
[14] Yang X, Cheng J H and Sun D W 2024 Enhancing microorganism inactivation performance through optimization of plate-to-plate dielectric barrier discharge cold plasma reactors *Food Control* **157** 110164
[15] Murata T, Suganuma R, Hashimoto M and Kubo K 2020 Engineering model of ozone generation considering microdischarges *IEEE Trans. Plasma Sci.* **48** 980–90
[16] Zhang C, Wang Y, Zhou Y, Xie Q, Wang R, Yan P and Shao T 2016 Electrical characteristics in surface dielectric barrier discharge driven by microsecond pulses *IEEE Trans. Plasma Sci.* **44** 2772–8
[17] Höft H, Becker M M, Kettlitz M and Brandenburg R 2022 Upscaling from single- to multi-filament dielectric barrier discharges in pulsed operation *J. Appl. Phys.* **55** 424003
[18] Malik M A, Schoenbach K H and Heller R 2014 Coupled surface dielectric barrier discharge reactor-ozone synthesis and nitric oxide conversion from air *Chem. Eng. J.* **256** 222–9
[19] Cimerman R and Hensel K 2023 Multi-hollow surface dielectric barrier discharge: production of gaseous species under various air flow rates and relative humidities *Plasma Chem. Plasma Process.* **43** 1411–33
[20] Wang Z *et al* 2022 Combination of NOx mode and O_3 mode air discharges for water activation to produce a potent disinfectant *Plasma Sources Sci. Technol.* **31** 05LT01
[21] Jodzis S and Baran K 2022 The influence of gas temperature on ozone generation and decomposition in ozone generator. How is ozone decomposed? *Vacuum* **195** 1
[22] Xi W, Wang W, Liu Z, Wang Z, Guo L, Wang X, Rong M and Liu D 2020 Mode transition of air surface micro-discharge and its effect on the water activation and antibacterial activity *Plasma Sources Sci. Technol.* **29** 095013
[23] Sung Y M and Sakoda T 2005 Optimum conditions for ozone formation in a micro dielectric barrier discharge *Surf. Coat. Technol.* **197** 148–53
[24] Murata T, Okita Y, Noguchi M and Takase I 2004 Basic parameters of coplanar discharge ozone generator *Ozone Sci. Eng.* **26** 429–42

[25] Shimizu T, Sakiyama Y, Graves D B, Zimmermann J L and Morfill G E 2012 The dynamics of ozone generation and mode transition in air surface micro-discharge plasma at atmospheric pressure *New J. Phys.* **14** 103028
[26] Warburg E and Leithäuser G 1906 Über die Oxydation des Stickstoffs bei der Wirkung der stillen Entladung auf die atmosphärische Luft *Ann. Phys.* **325** 743–50
[27] Kim M H, Cho J H, Park S J and Eden J G 2017 Modular and efficient ozone systems based on massively parallel chemical processing in microchannel plasma arrays: performance and commercialization *Eur. Phys. J. Spec. Top.* **226** 2923–44
[28] Korzec D, Neuwirth D and Nettesheim S 2021 Generation of negative air ions by use of piezoelectric cold plasma generator *Plasma* **4** 399–407
[29] Mandelbrot B B 1977 *Fractals : Form, Chance, and Dimension* (W.H. Freeman)
[30] Hota M K, Jiang Q, Mashraei Y, Salama K N and Alshareef H N 2017 Fractal electrochemical microsupercapacitors *Adv. Electron. Mater.* **3** 1700185
[31] Anagha P, Gopan G S S and Abraham N 2023 Simulation studies on the design and analysis of interdigital and fractal-based micro-supercapacitors *ECS J. Solid State Sci. Technol.* **12** 061003
[32] Syed A W and Mohammad M A 2021 Laser scribed graphene-based flexible microsupercapacitors with fractal design *IEEE Access* **9** 154957–64
[33] Alduais A A, Javaid A B, Syed M A and Rojas J P 2025 Analysis of electrodynamic screens with fractal designs for enhanced performance *Arab. J. Sci. Eng.* **50** 17575–85
[34] Charan K K S, Nagireddy S R, Bhattacharjee S and Hussain A M 2020 Design of heating coils based on space-filling fractal curves for highly uniform temperature distribution *MRS Adv.* **5** 1007–15
[35] Yang L, Yang F, Li K, Shen W, Xu T, Xu X, Zhou Y, Zhong M, Zheng M and Wei D 2021 Screen-printable and flexible in-plane micro-supercapacitors with fractal electrode design *Flex. Print. Electron.* **6** 025008
[36] Pei L, Zhuang P, Sun Y, Zhang X, Qiao H, Zhu K, Ajayan P M, Ye M and Shen J 2021 Nanosupercapacitors with fractal structures: searching designs to push the limit *J. Mater. Chem. A* **9** 17400–14
[37] Tiliakos A, Trefilov A M I, Tanasă E, Balan A and Stamatin I 2018 Space-filling supercapacitor carpets: highly scalable fractal architecture for energy storage *J. Power Sources* **384** 145–55
[38] Nguyen-Smith R T, Böddecker A, Schücke L, Bibinov N, Korolov I, Zhang Q Z, Mussenbrock T, Awakowicz P and Schulze J 2022 μs and ns twin surface dielectric barrier discharges operated in air: from electrode erosion to plasma characteristics *Plasma Sources Sci. Technol.* **31** 035008
[39] Li M, Zhu B, Yan Y, Li T and Zhu Y-M 2018 A high-efficiency double surface discharge and its application to ozone synthesis *Plasma Chem. Plasma Process.* **38** 1063–80
[40] Li M, Yan Y, Jin Q, Liu M, Zhu B, Wang L, Li T, Tang X J and Zhu Y M 2018 Experimental study on ozone generation from oxygen in double surface dielectric barrier discharge *Vacuum* **157** 249–58
[41] Amano I, Tanino M, Fujii N, Tanino Y, Takashima K and Mizuno A 2007 Sterilization using a wide-gap discharge formed by dielectric barrier discharge coupled with surface discharge under atmospheric pressure *2007 IEEE Industry Applications Annual Meeting* pp 1115–8
[42] Offerhaus B, Lackmann J W, Kogelheide F, Bracht V, Smith R, Bibinov N, Stapelmann K and Awakowicz P 2017 Spatially resolved measurements of the physical plasma parameters and the chemical modifications in a twin surface dielectric barrier discharge for gas flow purification *Plasma Process. Polym.* **14** e1600255
[43] Kogelheide F, Offerhaus B, Bibinov N, Krajinski P, Schücke L, Schulze J, Stapelmann K and Awakowicz P 2020 Characterisation of volume and surface dielectric barrier discharges in N_2–O_2 mixtures using optical emission spectroscopy *Plasma Process. Polym.* **17** e1900126
[44] Cheng L, Zhitao Z and Xiaofeng Z 2006 A study of the aging of a-Al_2O_3 dielectric material in DBD plasma *Plasma Sci. Technol.* **8** 693–6
[45] Hanson R E, Kimelman J, Houser N M and Lavoie P 2013 Effect of dielectric degradation on dielectric barrier discharge plasma actuator performance *51st AIAA Aerospace Sciences Meeting including the New Horizons Forum and Aerospace Exposition 2013*
[46] Avino F, Howling A A, Von Allmen M, Waskow A, Ibba L, Han J and Furno I 2023 Surface DBD degradation in humid air, and a hybrid surface-volume DBD for robust plasma operation at high humidity *J. Appl. Phys.* **56** 345201
[47] Ceh D Hilbert curve (Internet) (available at: http://a-d-c.ca/hilbert-curve/#page-content) (Accessed 25 August 2025)
[48] Pietsch G J 2001 Peculiarities of dielectric barrier discharges *Contrib. Plasma Phys.* **41** 620–8
[49] Takashima K, Zuzeek Y, Lempert W R and Adamovich I V 2011 Characterization of a surface dielectric barrier discharge plasma sustained by repetitive nanosecond pulses *Plasma Sources Sci. Technol.* **20** 055009
[50] Leonov S B, Adamovich I V and Soloviev V R 2016 Dynamics of near-surface electric discharges and mechanisms of their interaction with the airflow *Plasma Sources Sci. Technol.* **25** 063001
[51] Ren C, Huang B, Zhang C, Qi B, Chen W and Shao T 2023 Impact of surface charges on energy deposition in surface dielectric barrier discharge: a modeling investigation *Plasma Sources Sci. Technol.* **32** 025004
[52] Wang D, Jikuya M, Yoshida S, Namihira T, Katsuki S and Akiyama H 2007 Positive- and negative-pulsed streamer discharges generated by a 100-ns pulsed-power in atmospheric air *IEEE Trans. Plasma Sci.* **35** 1098–103
[53] Malik M A, Schoenbach K H, Abdel-Fattah T M, Heller R and Jiang C 2017 Low cost compact nanosecond pulsed plasma system for environmental and biomedical applications *Plasma Chem. Plasma Process.* **37** 59–76
[54] Iza F, Walsh J L and Kong M G 2009 From submicrosecond- to nanosecond-pulsed atmospheric-pressure plasmas *IEEE Trans. Plasma Sci.* **37** 1289–96
[55] Williamson J M, Trump D D, Bletzinger P and Ganguly B N 2006 Comparison of high-voltage ac and pulsed operation of a surface dielectric barrier discharge *J. Phys. D: Appl. Phys.* **39** 4400–6
[56] Machala Z, Janda M, Hensel K, Jedlovský I, Leštinská L, Foltin V, Martišovitš V and Morvová M 2007 Emission spectroscopy of atmospheric pressure plasmas for bio-medical and environmental applications *J. Mol. Spectrosc.* **243** 194–201
[57] Leonov S B, Petrishchev V and Adamovich I V 2014 Dynamics of energy coupling and thermalization in barrier discharges over dielectric and weakly conducting surfaces on μ s to ms time scales *J. Phys. D: Appl. Phys.* **47** 465201
[58] Jiang H and Shao T 2023 Surface dielectric barrier discharge driven by nanosecond pulses *Pulsed Discharge Plasmas* ed T Shao and C Zhang (Springer Nature Singapore) pp 635–72
[59] Pipa A V, Hoder T, Koskulics J, Schmidt M and Brandenburg R 2012 Experimental determination of dielectric barrier discharge capacitance *Rev. Sci. Instrum.* **83** 075111
[60] Bruggeman P, Walsh J L, Schram D C, Leys C and Kong M G 2009 Time dependent optical emission spectroscopy of submicrosecond pulsed plasmas in air with water cathode *Plasma Sources Sci. Technol.* **18** 045023

[61] Rathore V and Nema S K 2021 Optimization of process parameters to generate plasma activated water and study of physicochemical properties of plasma activated solutions at optimum condition *J. Appl. Phys.* **129** 084901
[62] Fan T, Chen Y, Zhang N, Wang Y, Wang X, Chang D and Yang K 2023 Nanosecond pulsed atmospheric-pressure plasma enhanced the germination of Melon (Cucumis melo L.) Seeds *Plasma Chem. Plasma Process.* **43** 1149–67
[63] Jin C, Lin F, Peng B, Wei L, Ling Z, Zeng X and Yuan D 2025 Nanosecond pulsed multi-hollow surface dielectric barrier discharge for ozone production *Vacuum* **238** 114252
[64] Bae J H, Lee H, Huh S C and Park S 2024 Nitric and nitrous acid formation in plasma-treated water: decisive role of nitrogen oxides (NOx=1–3) *Chemosphere* **364** 143105
[65] Martynenko A, Kudra T and Yue J 2017 Multipin EHD dryer: effect of electrode geometry on charge and mass transfer *Dry. Technol.* **35** 1970–80
[66] Li J Q, Yan H J, Li T, Yu S Q, Fan J W and Song J 2023 Surface charge characteristics in surface dielectric barrier discharge actuators with thin cylindrical exposed electrode *J. Appl. Phys.* **133** 063301
[67] Zerrouki A, Motomura H, Ikeda Y, Jinno M and Yousfi M 2016 Optical emission spectroscopy characterizations of micro-air plasma used for simulation of cell membrane poration *Plasma Phys. Control. Fusion* **58** 075006
[68] Ito Y, Sakai O and Tachibana K 2010 Measurement of electron density in a microdischarge-integrated device operated in nitrogen at atmospheric pressure using a millimetre-wave transmission method *Plasma Sources Sci. Technol.* **19** 025006
[69] Pekárek S and Mikeš J 2014 Temperature-and airflow-related effects of ozone production by surface dielectric barrier discharge in air *Eur. Phys. J. D* **68** 310
[70] Portugal S, Roy S and Lin J 2017 Functional relationship between material property, applied frequency and ozone generation for surface dielectric barrier discharges in atmospheric air *Sci. Rep.* **7** 6388
[71] Pipa A V, Hoder T and Brandenburg R 2013 On the role of capacitance determination accuracy for the electrical characterization of pulsed driven dielectric barrier discharges *Contrib. Plasma Phys.* **53** 469–80
[72] Zhuge Y, Liang J, Fu M, Long T and Wang H 2024 Comprehensive overview of power electronics intensive solutions for high-voltage pulse generators *IEEE Open J. Power Electron.* **5** 21–40
[73] Kogelschatz U 2003 Dielectric-barrier discharges: their history, discharge physics, and industrial applications *Plasma Chem. Plasma Process.* **23** 1–46
[74] De Meyer R, Verbeeck J, Bals S and Bogaerts A 2025 Contamination in dielectric barrier discharge plasmas by electrode erosion *ACS Mater. Lett.* **7** 52–58
[75] Warlitz P, Hehner M T, Pasch S, Serpieri J, Blank T and Kriegseis J 2024 On durable materials for dielectric-barrier discharge plasma actuators *Sens. Actuators A* **366** 114985
[76] Staack D, Farouk B, Gutsol A F and Fridman A 2007 Spatially resolved temperature measurements of atmospheric-pressure normal glow microplasmas in air *IEEE Trans. Plasma Sci.* **35** 1448–55
[77] Černák M, Černáková L, Hudec I, Kováčik D and Zahoranová A 2009 Diffuse coplanar surface barrier discharge and its applications for in-line processing of low-added-value materials *EPJ Appl. Phys.* **47** 22806
[78] Zhang L, Wang K, Wu K, Guo Y, Liu Z, Yang D, Zhang W, Luo H and Fu Y 2024 Air disinfection by nanosecond pulsed DBD plasma *J. Hazard. Mater.* **472** 134487